Integration of Polarimetric Decomposition, Object-Oriented Image Analysis, and Decision Tree Algorithms for Land-Use and Land-Cover Classification using RADARSAT-2 Polarimetric SAR Data

Zhixin Qi, Anthony G.O. Yeh, Xia Li, and Zheng Lin

Abstract

A novel method which integrates polarimetric decomposition, object-oriented image analysis, and decision tree algorithms is presented for land-use and land-cover (LULC) classification using RADARSAT-2 polarimetric SAR (POLSAR) data. Polarimetric decomposition which is aimed at extracting polarimetric parameters related to the physical scattering mechanisms of the observed objects can be used to support the classification of POLSAR data. The main purposes of object-oriented image analysis are delineating image objects as well as extracting various textural and spatial features from image objects to improve classification accuracy. A decision tree algorithm provides an efficient way to select features and implement classification. Compared with the Wishart supervised classification which is based on the coherency matrix, the proposed method can significantly improve the overall accuracy and kappa value of LULC classification by 17.45 percent and 0.24, respectively. Further investigation was carried out on the contribution of polarimetric decomposition, object-oriented image analysis, and decision tree algorithms to the improvement achieved by the proposed method. The investigation shows that all these three methods contribute to the improvement achieved by the proposed method.

Introduction

Land-use and land-cover (LULC) information is essential for urban planning and management. Remote sensing data obtained from different optical sensors have been commonly used to characterize and quantify LULC information (Imhoff *et al.*, 1997; Ridd and Liu, 1998; Sutton, 2003). However, conventional optical remote sensing is limited by weather conditions. Hence, it has difficulties in collecting timely LULC information in regions that are characterized by frequent cloud cover. Radar remote sensing, which is not affected by clouds, is therefore an effective tool for extracting timely LULC information in such regions.

Early studies on the use of radar remote sensing to investigate LULC information have been mainly based on airborne radar imagery and simple classification methods (Henderson, 1975; Henderson, 1977; Henderson, 1979). Many pioneer and detailed studies have been carried out using the space shuttle SIR-C/X-SAR (Kasischke *et al.*, 1997; Saatchi *et al.*, 1997; Pierce *et al.*, 1998). Although the results of these studies are positive, airborne radar imagery systems are only occasionally launched to collect experimental data within a very short period. Therefore, it is not practical to use airborne radar imagery to investigate timely LULC information. After the availability of operational orbital radar systems with SAR, such as the ERS-1 and ERS-2, JERS-1, and RADARSAT-1, the acquisition of timely LULC information using SAR images has become practical. However, most of the existing orbital SAR systems are single-frequency types and may create confusion during the separation and mapping of LULC classes; this confusion stems from the limited information obtained by single-frequency systems (Ulaby *et al.*, 1986; Leiss *et al.*, 1996; Li and Yeh, 2004).

To overcome the difficulty presented by single-frequency SAR data, some researchers utilized polarimetric SAR (POLSAR) data to extract LULC information (Pierce *et al.*, 1994; Du and Lee, 1996; Lee *et al.*, 2001; Freitas *et al.*, 2008). The results show that POLSAR measurements achieve better classification results than single-polarization SAR. The classification of POLSAR images has become an important research topic since POLSAR data have been made available through ENVISAT ASAR, ALOS PALSAR, and RADARSAT-2. Classification methods for POLSAR images have been examined by many researchers (Rignot *et al.*, 1992; Hara *et al.*, 1994; Chen *et al.*, 1996; Tzeng and Chen, 1998; Barnes and Burki, 2006). Recently, some polarimetric decomposition theorems have been examined (Cloude and Pottier, 1996; Freeman and Durden, 1998; Yang *et al.*, 1998; Carrea and Wanielik, 2001; Cameron and Rais, 2006), and classification methods based on decomposition results have been examined (Cloude and Pottier, 1997; Lee *et al.*, 1999a; Pottier and Lee, 1999; Ferro-Famil *et al.*, 2001). Thus far, however, most of the classification

Zhixin Qi and Anthony G.O. Yeh are with the Department of Urban Planning and Design, The University of Hong Kong, Pokfulam Road, Hong Kong SAR, P.R. China (qizhixin@hku.hk).

Xia Li and Zheng Lin are with the School of Geography and Planning, Sun Yat-sen University, 135 West Xingang Rd., Guangzhou 510275, P.R. China.

Photogrammetric Engineering & Remote Sensing
Vol. 78, No. 2, February 2012, pp. 169–181.

0099-1112/12/7802–169/$3.00/0

methods for POLSAR images are pixel-based and can only utilize the tonal information of pixels. Purely pixel-based approaches have limitations in representing objects in high-resolution images; thus, they have difficulties in utilizing the textural and spatial information of POLSAR images. Moreover, the results of pixel-based methods are insufficient for extracting objects of interest and expediently updating geographical information system databases.

Object-oriented image analysis has been increasingly used for the classification of remote sensing data (Evans *et al.*, 2002; Geneletti and Gorte, 2003; Gao *et al.*, 2006; Li *et al.*, 2008; Li *et al.*, 2009; Watts *et al.*, 2009). In object-oriented image analysis, a feature is an attribute that represents information concerning the objects under study. Given that regions in an image provide considerably more information than do pixels, many different image object features for measuring the color, shape, and texture of the associated regions can be used. By delineating objects from remote sensing images, object-oriented image analysis enables the acquisition of a variety of additional spatial and textural features, which are important for improving the accuracy of remote sensing classification (Benz *et al.*, 2004). Furthermore, image objects are much easier to manipulate and utilize than in pixels. However, with the addition of textural and spatial features, hundreds of features can potentially be incorporated into the object-oriented classification of POLSAR data. Therefore, feature selection presents a problem in the object-oriented classification of POLSAR data. Using all available features in classification is improper because computation is intensive and some features may degrade classification performance. Since the recent introduction of polarimetric decomposition theorems, which have brought about much more polarimetric information, the problem of feature selection has become more intractable.

Decision tree algorithms can be used to solve the problem of feature selection. Decision trees are commonly used for the selection of variables in classification (Lawrence and Wright, 2001). By examining the effects of every input feature to determine every split in the final tree, decision tree algorithms can efficiently deal with the problem of feature selection in classification. Some studies have shown that decision trees can provide an accurate and efficient method for LULC classification with remote sensing (Friedl and Brodley, 1997; Swain and Hauska, 1977; McIver and Friedl, 2002; Kandrika and Roy, 2008). The improvement achieved by the integration of object-oriented image analysis and decision tree algorithms in the classification of multispectral optical data has been demonstrated (Watts *et al.*, 2009). However, there is still a general lack of studies on the integration of these two methods for the classification of POLSAR data.

The objective of this study is to examine a new method for LULC classification using RADARSAT-2 POLSAR data. The new method is based on the integration of polarimetric decomposition, object-oriented image analysis, and decision tree algorithms. First of all, polarimetric parameters were extracted using the Pauli and H/A/Alpha decompositions. Next, the extracted polarimetric parameters were combined with the backscattering matrix elements and the coherency matrix elements to form a multichannel image. Then, during the object-oriented image analysis, image objects were delineated by implementing multi-resolution segmentation on the Pauli color-coded image of RADARSAT-2 POLSAR data. Meanwhile, a total of 1,161 features were extracted from each image object. After this, a decision tree algorithm was used to select features and create a decision tree for the LULC classification. Finally, the LULC classification was implemented using the constructed decision tree.

Study Area and Data

The study area is in Panyu District of Guangzhou City in Southern China with latitudes 22°51′ to 22°58′ and longitudes 113°20′ to 113°33′ (Figure 1). Panyu lies at the heart of the Pearl River Delta. It has a total land area of 1,314 km^2 as well as a population of 926,542. This district was an agricultural area before the economic reform in 1978, but has been transformed recently into an urban area. Since Panyu became a district of Guangzhou in July 2000, intensive land development has been implemented to provide housing to the residents of Guangzhou City. Huge profits have been generated through property development, which resulted in the increase in land speculation activities and illegal land development. Some illegal land development projects have caused irreversible environmental problems, such as forest degradation, soil erosion, and adverse effects on species diversity. Timely and accurate LULC information is important for the local government to create management policies for the control and prevention of illegal development at its early stage.

RADARSAT-2 is the world's most advanced commercial C-band SAR satellite. It follows the same orbit, repeat cycle, and ground track as RADARSAT-1. RADARSAT-2 is designed with significant and powerful technical advancements, one of which is multi-polarization. RADARSAT-1 provides horizontal-transmit and horizontal-receive (HH) data only, while RADARSAT-2 can transmit horizontal (H) and vertical (V) polarizations depending on the selected mode. Each scattering element (HH, VV, HV, and VH) has varying sensitivities to different surface characteristics and properties, thereby helping to improve the discrimination among different LULC types. As RADARSAT-2 is a newly launched sensor, the quantitative investigation on the potential of RADARSAT-2 POLSAR data in LULC classification is still lack. In this study, a RADARSAT-2 Fine Quad-Pol image (Single Look Complex) acquired on 21 March 2009 was used for extracting LULC information (Plate 1a). The image has a full polarization of HH, HV, VH, and VV, a resolution of 5.2 m × 7.6 m, and an incidence angle of 31.5°.

LULC classes in the study area can be summarized into four categories: built-up area, water, barren land, and vegetation. The field investigation was carried out simultaneously with the acquisition of the RADARSAT-2 image to

Figure 1. Study area for LULC classification using RADARSAT-2 POLSAR data in Guangzhou.

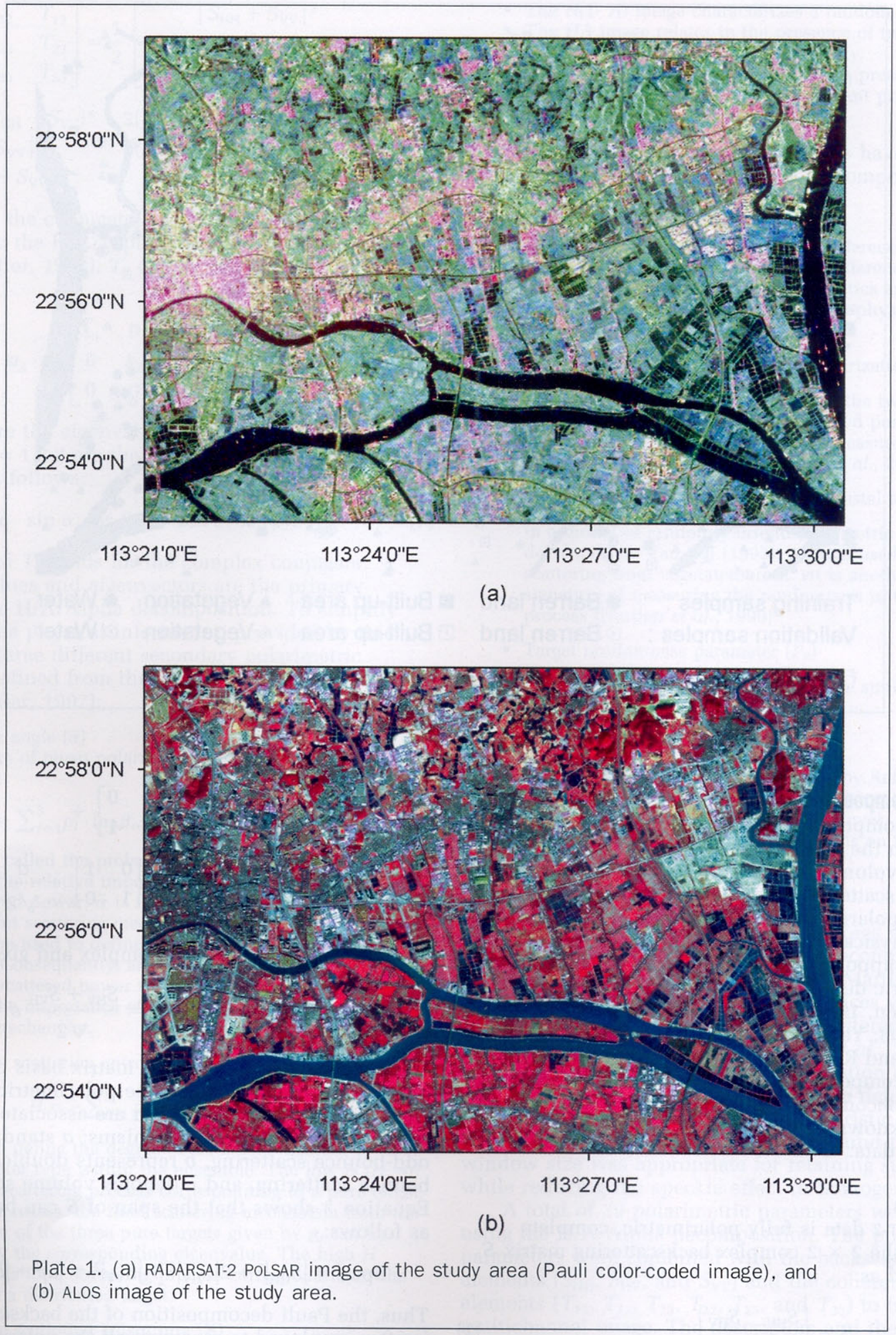

Plate 1. (a) RADARSAT-2 POLSAR image of the study area (Pauli color-coded image), and (b) ALOS image of the study area.

collect ground truth. An ALOS image of the 10-meter multispectral bands, acquired on 31 November 2008, was used as a reference map to facilitate the collection of ground truth (Plate 1b). In the field investigation, a total of 402 field plots were selected across typical LULC classes using a clustered sampling approach (McCoy, 2005). In terrain with poor access, this sampling approach enables the use of most of the accessible sites. GPS was used to record the coordinates of these field plots. On the basis of the experience with multinomial distribution (Congalton and Green, 2009), a minimum of 50 samples were collected for each category. The sampling size per field plot in the image ranged from 39 to 603 pixels, which was determined using the ground coverage in the photos taken during the fieldwork. The collected field plots were divided into two groups for training and validation. There were 200 plots in the training group and 202 plots in the validation group (Figure 2). The first group was used to select features and create a decision tree for classification, while the second group was used to verify the results of the classification.

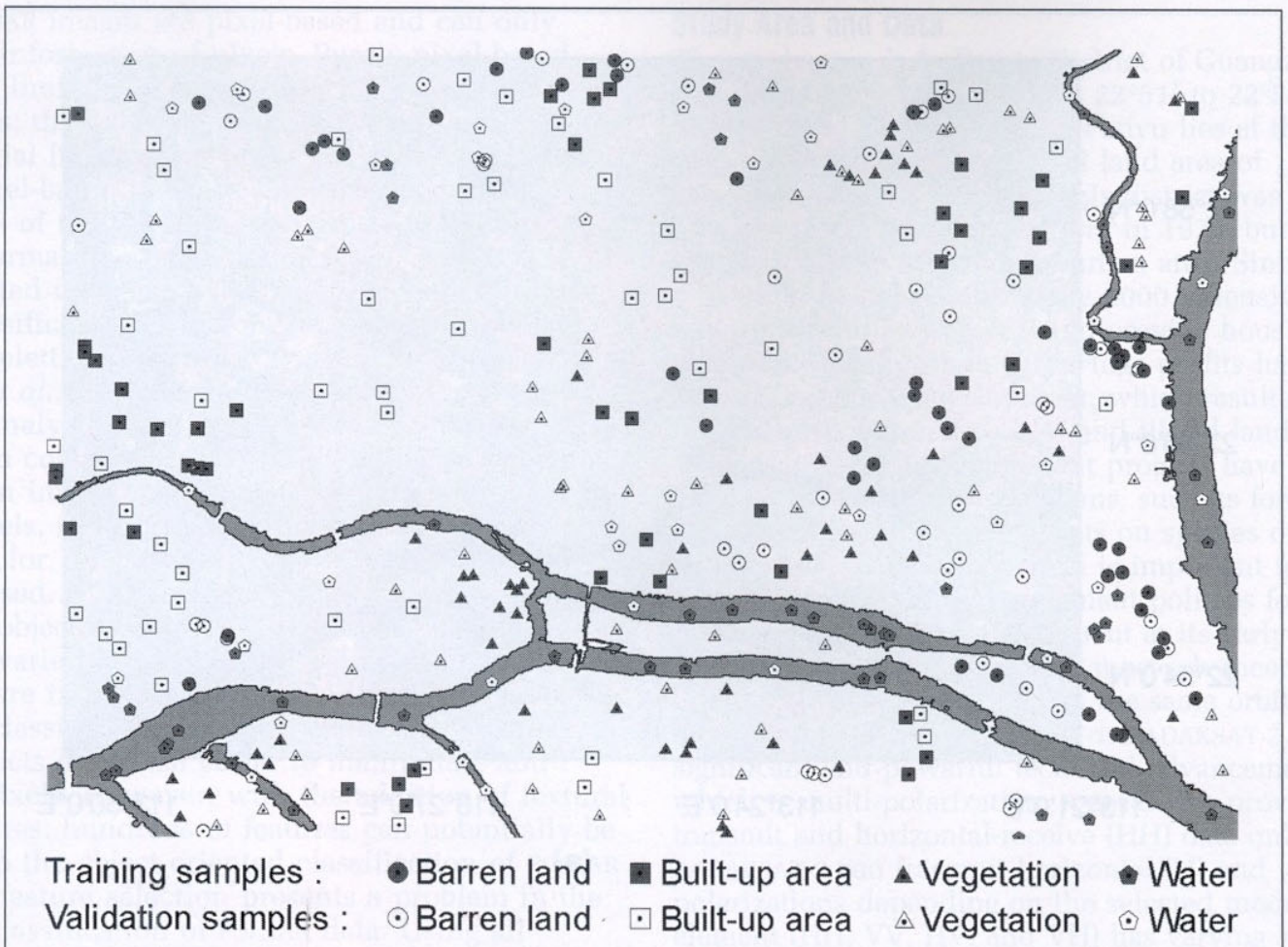

Figure 2. Collected samples across typical LULC classes in the study area.

Polarimetric Decomposition

Polarimetric decomposition is aimed at extracting physical information from the observed scattering of microwaves by the surface and volume structures of ground objects for the classification of scattering data. The polarimetric parameters extracted using polarimetric decomposition techniques are related to the physical properties of the observed targets and can be used to support the classification of POLSAR data. Many polarimetric decomposition methods have been proposed (Huynen, 1970; Cloude and Pottier, 1996; Freeman and Durden, 1998; Yang *et al.*, 1998; Carrea and Wanielik, 2001; Cameron and Rais, 2006). In this study, the focus was on the Pauli decomposition (Cloude and Pottier, 1996) and the H/A/Alpha decomposition (Cloude and Pottier, 1997), which are well-known decomposition methods commonly used for POLSAR data.

Pauli Decomposition

As the RADARSAT-2 data is fully polarimetric, complete information on the 2 × 2 complex backscattering matrix $\boldsymbol{S}$ can be expressed as:

$$\mathbf{S} = \begin{bmatrix} S_{HH} & S_{HV} \\ S_{VH} & S_{VV} \end{bmatrix} \tag{1}$$

where S_{HH} and S_{VV} denote the copolarized complex scattering amplitudes, and S_{HV} and S_{VH} denote the cross-polarized complex scattering amplitudes. The total received power from the four polarimetric channels is referred to as "span." If the transmit and receive antennas coincide, the backscattering matrix may be symmetric, with $S_{HV} = S_{VH}$.

In the Pauli decomposition, backscattering matrix $\boldsymbol{S}$ is expressed as the complex sum of the Pauli matrices (Cloude and Pottier, 1996):

$$\mathbf{S} = \begin{bmatrix} S_{HH} & S_{HV} \\ S_{VH} & S_{VV} \end{bmatrix} = \frac{a}{\sqrt{2}} \begin{bmatrix} 1 & 0 \\ 0 & 1 \end{bmatrix} + \frac{b}{\sqrt{2}} \begin{bmatrix} 1 & 0 \\ 0 & -1 \end{bmatrix} + \frac{c}{\sqrt{2}} \begin{bmatrix} 0 & 1 \\ 1 & 0 \end{bmatrix} + \frac{d}{\sqrt{2}} \begin{bmatrix} 0 & -j \\ j & 0 \end{bmatrix} \tag{2}$$

where a, b, c, and d are all complex and given by:

$$a = \frac{S_{HH} + S_{VV}}{\sqrt{2}} \quad b = \frac{S_{HH} - S_{VV}}{\sqrt{2}} \quad c = \frac{S_{HV} + S_{VH}}{\sqrt{2}} \quad d = j\frac{S_{HV} - S_{VH}}{\sqrt{2}}. \tag{3}$$

Because $S_{HV} = S_{VH}$, the Pauli matrix basis can be reduced to the first three matrices. The polarimetric parameters from the Pauli decomposition are associated for three elementary scattering mechanisms: a stands for single- or odd-bounce scattering, b represents double- or even-bounce scattering, and c denotes volume scattering. Equation 3 shows that the span of $\boldsymbol{S}$ can be obtained as follows:

$$\text{Span} = |S_{HH}|^2 + 2|S_{HV}|^2 + |S_{VV}|^2 = |a|^2 + |b|^2 + |c|^2. \tag{4}$$

Thus, the Pauli decomposition of the backscattering matrix is often employed to represent all the polarimetric information in a SAR image. As shown in Plate 1a, a Pauli color-coded image can be formed with intensities $|a|^2$ (Blue), $|b|^2$ (Red), $|c|^2$ and (Green), which correspond to clear physical scattering mechanisms.

H/A/Alpha Decomposition

The backscattering matrix elements can be arranged into a vector: $\boldsymbol{k} = 0.707\ [S_{HH} + S_{VV},\ S_{HH} - S_{VV},\ 2S_{HV}]$ with the tree elements referred to as the Pauli components of the signal. The 3 × 3 coherency matrix $\boldsymbol{T}_3$ is defined as the expected value of $\boldsymbol{kk}^{*T}$ (Lee and Poitter, 2009).

$$\boldsymbol{T}_3 = \begin{bmatrix} T_{11} & T_{12} & T_{13} \\ T_{12}^* & T_{22} & T_{23} \\ T_{13}^* & T_{23}^* & T_{33} \end{bmatrix} = \frac{1}{2} \begin{bmatrix} |S_{HH} + S_{VV}|^2 & (S_{HH} + S_{VV})(S_{HH} - S_{VV})^* & 2(S_{HH} + S_{VV})S_{HV}^* \\ (S_{HH} - S_{VV})(S_{HH} + S_{VV})^* & |S_{HH} - S_{VV}|^2 & 2(S_{HH} - S_{VV})S_{HV}^* \\ 2S_{HV}(S_{HH} + S_{VV})^* & 2S_{HV}(S_{HH} - S_{VV})^* & 4|S_{HV}|^* \end{bmatrix} \quad (5)$$

where * denotes the conjugate, and || denotes the module.

According to the H/A/Alpha decomposition theorem (Cloude and Pottier, 1997), $\boldsymbol{T}_3$ can be decomposed as follows:

$$\boldsymbol{T}_3 = [\underline{\boldsymbol{u}}_1 \ \underline{\boldsymbol{u}}_2 \ \underline{\boldsymbol{u}}_3] \begin{bmatrix} \lambda_1 & 0 & 0 \\ 0 & \lambda_2 & 0 \\ 0 & 0 & \lambda_3 \end{bmatrix} [\underline{\boldsymbol{u}}_1 \ \underline{\boldsymbol{u}}_2 \ \underline{\boldsymbol{u}}_3]^1 \quad (6)$$

where λ_1 λ_2 λ_3 are the eigenvalues of $\boldsymbol{T}_3$, and $\infty > \lambda_1 > \lambda_2 > \lambda_3 > 0$; $\underline{\boldsymbol{u}}_i$ for I = 1,2,3 are the eigenvectors of $\boldsymbol{T}_3$, and can be formulated as follows:

$$\underline{u}_i = [\cos\alpha_i \ \ \sin\alpha_i \cos\beta_i e^{j\delta_i} \ \ \sin\alpha_i \cos\beta_i e^{j\delta_i}]^T \quad (7)$$

where the symbol T stands for the complex conjugate.

The eigenvalues and eigenvectors are the primary parameters of the H/A/Alpha decomposition. To simplify the analysis of the physical information provided by this decomposition, three different secondary polarimetric parameters are defined from the eigenvalues and eigenvectors (Cloude and Pottier, 1997):

- Mean alpha angle ($\bar{\alpha}$)
  The estimate of mean polarimetric parameter α_i, β_i, γ_i, δ_i set is given by:

$$(\bar{\alpha},\bar{\beta},\bar{\gamma},\bar{\delta}) = \sum_{i=1}^{3} p_i \cdot (\alpha_i,\beta_i,\gamma_i,\delta_i) \ p_i = \lambda_i / \sum_{k=1}^{3} \lambda_k \quad (8)$$

  where p_i is called the probability of eigenvalue λ_i, and represents the relative importance of this eigenvalue to the total scattered power; $\bar{\alpha}$ is the main parameter for identifying the dominant scattering mechanism. The other parameters $\bar{\beta},\bar{\gamma},\bar{\delta}$ can be used to define the target polarization orientation angle. Consequently, an eigenvalue corresponds to the associated scattered power to the corresponding eigenvector and gives the importance of the corresponding eigenvector or scattering mechanism.

- Polarimetric scattering entropy (H)

$$H = -\sum_{i-1}^{3} p_i \log_3 p_i \quad (9)$$

  H is used to define the degree of statistical disorder of each distinct scatter type within the ensemble. The low H ($H \rightarrow 0$) indicates a scattering process corresponding to a pure target. As the H increases, the final scattering mechanism from the combination of the three pure targets given by $\underline{\boldsymbol{u}}_i$ can be weighted by the corresponding eigenvalue. The high H ($H \rightarrow 1$) stands for a scattering process corresponding to the response of a distributed target.

- Polarimetric scattering anisotropy (A)

$$A = (\lambda_2 - \lambda_3)/(\lambda_2 + \lambda_3) \quad (10)$$

  A is a parameter complementary to the entropy. It measures the relative importance of the second and the third eigenvalues of the H/A/Alpha decomposition.

Some combinations between H and A were proposed to improve the capability to distinguish different types of scattering processes (Lee and Poitter, 2009):

- The (1- H)(1- A) image corresponds to the presence of a single dominant scattering process.
- The H(1- A) image characterizes a random scattering process.
- The HA image relates to the presence of two scattering mechanisms with the same probability.
- The (1- H)A image corresponds to the presence of two scattering mechanisms with a dominant process and a second one with medium probability.

Some other polarimetric parameters have been proposed based on the use of the H/A/Alpha decomposition.

- SERD and DERD

  Single bounce eigenvalue relative difference (SERD) and double bounce eigenvalue relative difference (DERD) are sensitive to natural media characteristics and can be used for quantitative inversion of bio- and geo-physical parameters (Allain *et al.*, 2004).

- Polarization asymmetry (PA) and polarization fraction (PF)

  PA measures the relative strength of the two polarimetric scattering mechanisms in the polarized portion of radar return (Ainsworth *et al.*, 2000). PF measures the unpolarized portion of radar return (Ainsworth *et al.*, 2002).

- Radar vegetation index (RVI) and pedestal height (PH)

  In a model of randomly oriented dielectric cylinders developed by Van Zyl (1992), RVI was used for analyzing the scattering from vegetated areas. PH is another polarization signature of measuring the randomness in the scattering process (Durden *et al.*, 1990).

- Target randomness parameter (P_R)

  P_R is very close to H and provides the similar information (Luneburg, 2001).

- Shannon entropy (SE)

  This parameter has been introduced by Refregier (2006) as a sum of SE_I and SE_P. SE_I is the intensity contribution that depends on the total backscattered power, and SE_P is the polarimetric contribution that depends on the Barakat degree of polarization.

Polarimetric Parameter Extraction

The PolSARPro, ver. 4.03 software package was used to implement the Pauli and H/A/Alpha decompositions to extract polarimetric parameters (López-Martínez *et al.*, 2005). The backscattering and coherency matrices were generated from the RADARSAT-2 POLSAR data and filtered using the refined Lee POLSAR speckle filter (Lee *et al.*, 1999b), which is good at preserving polarimetric information and the correlation between polarization channels. The determination of the window size of the filter was a heuristic process. By trying different window sizes, it was found that a 5×5 window size was appropriate for retaining subtle details while reducing the speckle effect in homogeneous areas.

A total of 39 polarimetric parameters were extracted using the H/A/Alpha decomposition. The polarimetric parameters were combined with the backscattering matrix elements (S_{HH}, S_{HV}, and S_{VV}) and the coherency matrix elements (T_{11}, T_{12}, T_{13}, T_{22}, T_{23}, and T_{33}) to form a POLSAR multichannel image. The descriptors and the corresponding image channels are listed in Table 1. The next step was to delineate image objects and extract their features from the multichannel image using object-oriented image analysis.

Object-oriented Image Analysis for PolSAR Images

One way to compensate for the limited information from single frequency SAR data is to derive more features, such as texture and shape of objects, for the classification of SAR images in addition to the backscatter coefficients. Object-oriented image analysis can be used on SAR images to extract such type of information. The object-oriented

TABLE 1. DESCRIPTORS AND CORRESPONDING IMAGE CHANNELS OF THE POLSAR MULTICHANNEL IMAGE

Channel	Descriptor				Description
1-3	S_{HH}	S_{HV}	S_{VV}		Backscattering matrix elements
4-9	T_{11}	T_{12}	T_{13}	T_{22}	Coherency matrix elements
	T_{23}	T_{33}			
10-13	$\bar{\lambda}$	λ_1	λ_2	λ_3	Eigenvalues of H/A/Alpha decomposition
14-16	p_1	p_2	p_3		Probability of eigenvalues
17-20	α_1	α_2	α_3	$\bar{\alpha}$	Alpha angles and their mean value
21-24	β_1	β_2	β_3	$\bar{\beta}$	Beta angles and their mean value
25-28	δ_1	δ_2	δ_3	$\bar{\delta}$	Delta angles and their mean value
29-32	γ_1	γ_2	γ_3	$\bar{\gamma}$	Gamma angles and their mean value
33-38	H	A	$(1\text{-}H)A$	$H(1\text{-}A)$	Polarimetric scattering entropy, polarimetric scattering anisotropy, and their combinations
	HA	$(1\text{-}H)(1\text{-}A)$			
39	SERD				Single bounce eigenvalue relative difference
40	DERD				Double bounce eigenvalue relative difference
41	PA				Polarization asymmetry
42	PF				Polarization fraction
43	RVI				Radar vegetation index
44	PH				Pedestal height
45	P_R				Target randomness parameter
46-48	SE	SE_I	SE_P		Shannon entropy

package Definiens Developer 7.0 (previously called eCognition) was used to implement object-oriented image analysis in this study. There are two steps in object-oriented image analysis: (a) image segmentation, and (b) feature extraction.

Multi-resolution Segmentation of PolSAR Images

Multi-resolution segmentation (Uchiyama and Arbib, 1994; Benz *et al.*, 2004) was used to delineate image objects from the RADARSAT-2 POLSAR image. The POLSAR multichannel image consists of as many as 48 channels; thus, the selection of appropriate channels for multi-resolution segmentation is necessary. Using all the channels in image segmentation is improper given that some channels may degrade segmentation results because of the high noise in these channels. For example, considerable noise exists in some polarimetric parameters, such as scattering anisotropy and alpha angles. Although these polarimetric parameters may represent important information for identifying some LULC classes, they are inappropriate for image segmentation because of their poor ability to display the accurate boundaries of land parcels and subtle details. Moreover, the increase in image channels in segmentation process results in much more computation time. Therefore, in this study, the image segmentation was implemented on the Pauli color-coded image to delineate objects. As previously mentioned, the Pauli color-coded image has become the standard for POLSAR image display because it can represent all the polarimetric information in a POLSAR image. Moreover, the Pauli color-coded image represents clear physical scattering mechanisms, which allow for clear contrast among different LULC types. Given that the three channels of the Pauli color-coded image correspond to the three elementary scattering mechanisms with the same importance, equal weight was assigned to the three channels in the image segmentation.

Multi-resolution segmentation is a bottom-up, region-merging technique that begins with one-pixel objects. During the region-merging process, smaller image objects are merged into larger ones, and a heuristic optimization procedure is used to minimize the weighted heterogeneity of the resultant image objects. Heterogeneity is determined using the standard deviation of color properties and their shapes as basis. The merging of a pair of adjacent image objects increases heterogeneity. The process will stop if the growth exceeds the threshold defined by a so-called scale parameter. Adjusting the scale parameter indirectly influences the average object size, i.e., a higher value leads to larger objects and vice versa. Setting the scale parameter was a heuristic process. Multi-resolution segmentation with different scale parameters was carried out to determine the optimal scale parameter. The corresponding segmentation results related to the different scale parameters are shown in Plate 2. The experiment shows that the segmentation with a scale parameter of 10 was good enough for delineating accurate land parcels and retaining subtle details. Image objects became too fragmental at a scale parameter smaller than 10.

Feature Extraction from the PolSAR Multichannel Image

Object-oriented image analysis provides useful additional information for separating different LULC classes. Because the multichannel image consists of as many as 48 channels, the number of features that can be extracted from one image object is as high as 1,161. These features are the indigenous parameters of Definiens Developer 7.0, and they are listed as four major categories (Baatz *et al.*, 2004):

1. 192 (4×48) indicators related to the statistical values of each object: min, max, mean, and standard deviation of each layer;
2. 576 (12×48) indicators related to texture (e.g., grey-level co-occurrence matrix (GLCM) homogeneity, GLCM contrast, GLCM dissimilarity, and GLCM entropy);
3. 336 (7×48) indicators related to spatial relationship (e.g., mean difference to neighbors and mean difference to brighter neighbors);
4. 57 indicators related to shape (e.g., area, length, number of segments, and main line curvature/length extracted from an image object).

Classification Using Decision Tree Algorithms

The main task of this step is to determine the class of each image object based on their features. As a large set of features were extracted from image objects through object-oriented image analysis, the determination of the features used in classification is very important. Decision trees are used to predict the membership of cases or objects in the classes of a categorical dependent variable based on their measurements on one or more predictor variables. Decision trees are not just feature selection methods like principal component analysis (PCA). They are generally used with full dimensionality of data to achieve a final classification. By examining

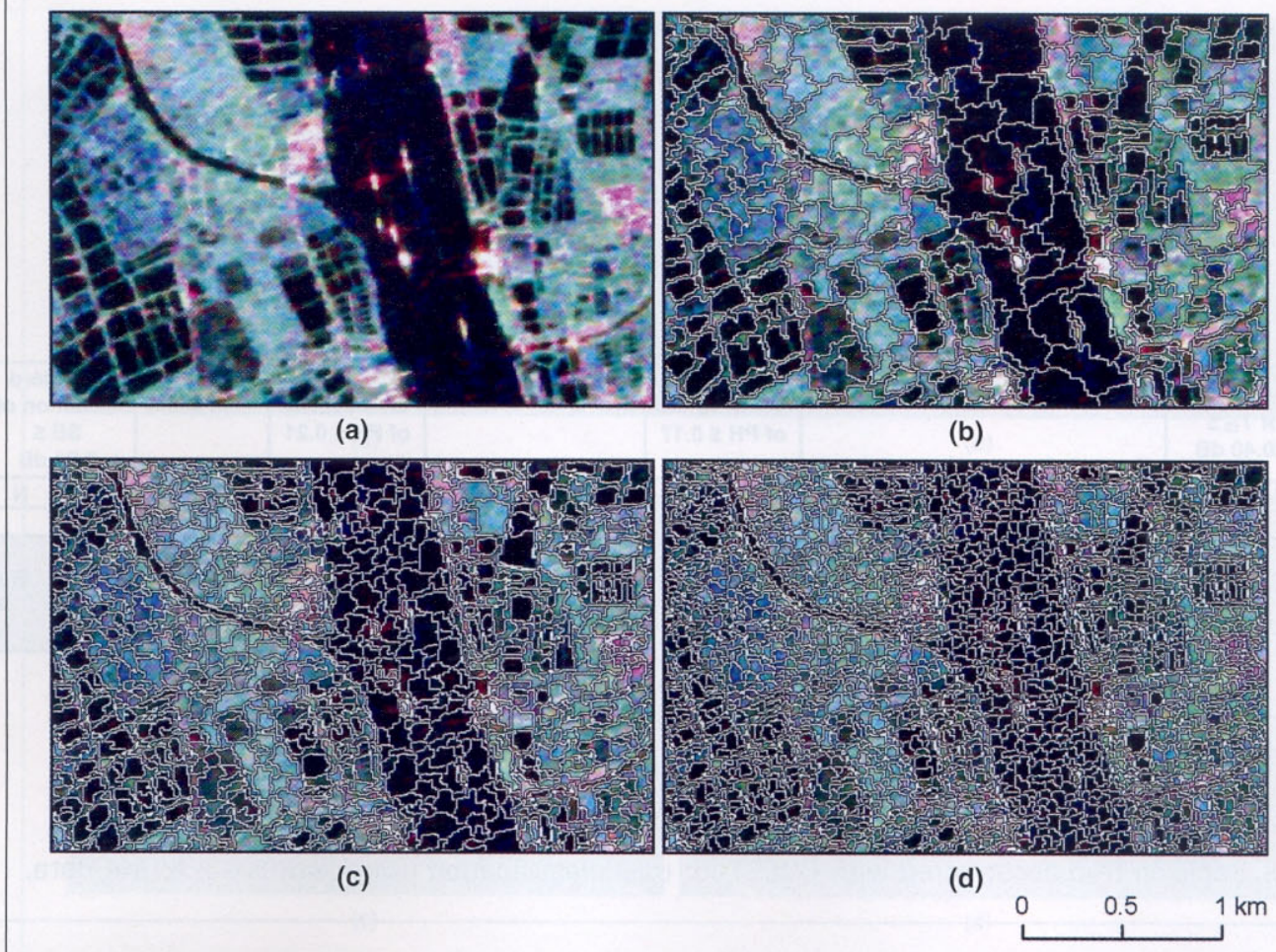

Plate 2. Determination of the optimal scale parameter for the segmentation of the Pauli color-coded image of RADARSAT-2 POLSAR image: (a) No Segmentation, (b) Scale = 20, (c) Scale = 10, and (d) Scale = 5.

the effects of every input feature to determine every split in the final tree, decision trees can select the most important features that achieve the best classification result.

Classification accuracies from decision tree classifiers are often greater as compared with those obtained using the maximum likelihood or linear discriminant function classifiers (Laliberte *et al.*, 2006). Decision tree algorithms have many advantages: (a) They are white box models that are simple to understand and interpret. If a given result is provided by the model, the result is easily interpreted by simple mathematics; (b) By performing univariate splits and examining the effects of predictors one at a time, decision trees are able to handle a variety of types of predictors, such as numerical or categorical predictors, and require little data preparation; and (c) They are robust and perform well with large data set in a short period of time.

In this study, QUEST (Loh and Shih, 1997; Lim *et al.*, 2000; Wu *et al.*, 2009) was used as a decision tree tool to implement classification. QUEST is a binary-split decision tree algorithm for classification and data mining. Training objects were manually drawn on the Pauli color-coded image based on the field plots in the training group. After the implementation of the image segmentation, the training objects were further segmented into a large number of sub-objects. More than 1,000 training objects were acquired for the construction of the decision trees. On the basis of the training objects, a decision tree was constructed using QUEST for the LULC classification. To remove the sections of the decision tree that may have arisen from noisy or erroneous data, the decision tree was pruned with 10-fold cross-validation and the 1-SE rule; these are common methods for pruning decision trees and are embedded in QUEST. The final decision tree constructed using QUEST is shown in Figure 3, and the selected features in the final tree are listed as follows:

- Layer mean values of T_{13}, T_{23}, T_{33}, α_2, and PH

  The mean value of an image object that consists of n pixels in channel c is calculated from the value of the pixels (c_i).

$$m_c = \frac{1}{n}\sum_{i=1}^{n} c_i \tag{11}$$

- Standard deviation of T_{13} and SE

  The standard deviation of an image object that consists of n pixels in channel c is calculated from the value of the pixels (c_i).

$$\sigma_c = \sqrt{\frac{1}{n}\left(\sum_{i=1}^{n} c_i^2 - \frac{1}{n}\sum_{i=1}^{n} c_i \sum_{i=1}^{n} c_i\right)} \tag{12}$$

- GLCM Ang. 2nd moment of T_{12} and PH

  GLCM is a tabulation of how often different combinations of pixel gray levels occur in an image. GLCM Ang. 2nd moment measures the local homogeneity. The value is high if some elements are large and the remaining ones are small.

$$\text{GLCM Ang.2}^{\text{nd}}\text{ moment} = \sum_{i,j=0}^{N-1} P_{i,j}^2 \tag{13}$$

  where i is the row number, j is the column number in the texture calculation cell matrix, N denotes the number of rows or columns of the cell matrix, and $P_{i,j}$ is the normalized value in cells i and j, and is defined as:

$$P_{i,j} = \frac{V_{i,j}}{\sum_{i,j=0}^{N-1} V_{i,j}} \tag{14}$$

where $V_{i,j}$ is the value in cells i and j of the image window.

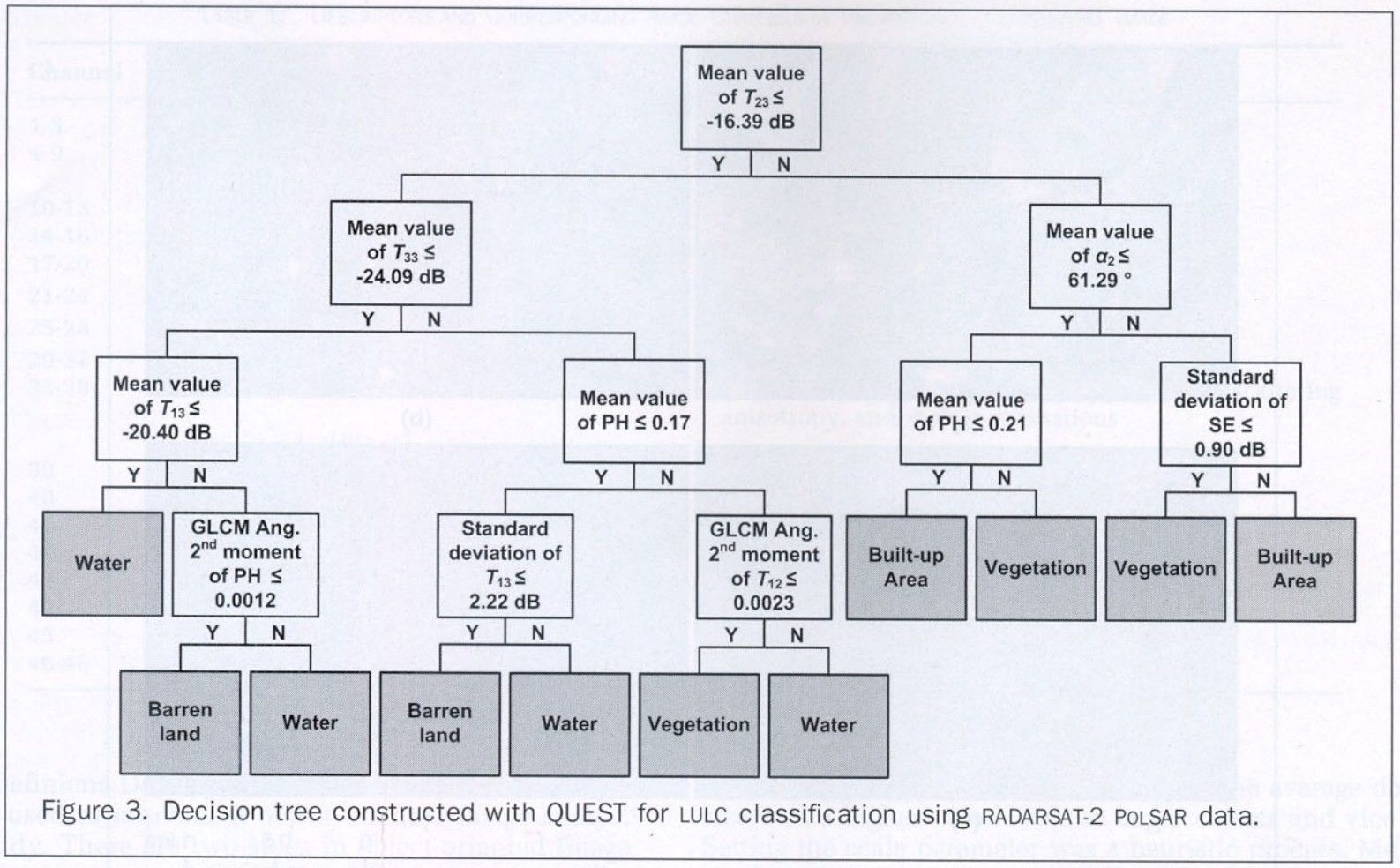

Figure 3. Decision tree constructed with QUEST for LULC classification using RADARSAT-2 POLSAR data.

Figure 3 shows that no spatial or geometric feature was selected in the final tree. The main reason is that the image objects delineated from the image segmentation were too fragmental to represent unbroken land parcels. As a land parcel in SAR images is not as homogeneous as that in optical images because of speckle in POLSAR images, the small scale parameter had to be used in the multi-resolution segmentation to delineate the accurate boundaries of land parcels and retain subtle details. However, the small scale parameter also led to an over segmentation of the image, resulting in a large number of fragmental image objects. As shown in Plate 2, some land parcels were segmented into many fragmental parts (image objects). An image object usually represents part of a land parcel; thus, using the spatial or geometric information on land parcels was difficult.

Results of Classification and Validation

A comparison between the proposed method and the Wishart supervised classification which is based on the coherency matrix (Lee *et al.*, 1994; Pottier *et al.*, 2005) was made to test the performance of the proposed method (Plate 3). The Wishart supervised classification is commonly used for the classification of POLSAR data. This method is a pixel-based maximum likelihood classifier based on the complex Wishart distribution for the coherency matrix. The Wishart supervised classification was implemented using the PolSARPro, ver. 4.03 software (López-Martínez *et al.*, 2005). A total of 37,615 pixels of ground data were collected for the validation of the classification results. Based on the confusion matrix determined using the validation set, four statistics are calculated for the validation: overall accuracy, estimate of kappa (Kappa), producer's accuracy, and user's accuracy (Story and Congalton, 1986; Congalton and Green, 2009). The accuracy statistics of these two methods is provided in Tables 2 and 3. The overall accuracy of the proposed method was 92.17 percent, whereas that of the Wishart supervised classification was 74.72 percent. The kappa value of the proposed method was 0.90, much higher than that of the Wishart supervised classification, which exhibited a kappa value of 0.66. Furthermore, the proposed method achieved higher producer's and user's accuracies for almost all the classes than did the Wishart supervised classification, especially for built-up area and vegetation. The results show that a great improvement was achieved using the proposed method compared with the Wishart supervised classification. However, the comparison only shows the improvement achieved by using the H/A/Alpha decomposition, object-oriented image analysis, and decision tree algorithms. Additional comparisons were made to investigate the detailed contribution of these three methods to the improvement.

Classification using object-oriented image analysis and decision tree algorithms but without the H/A/Alpha decomposition was implemented based on the backscattering matrix and the coherency matrix. The classification result and the accuracy evaluation are shown in Plate 3c and Table 4. The comparison between the method without the H/A/Alpha decomposition and the proposed method shows the contribution of the H/A/Alpha decomposition to the final accuracy of the proposed method. The overall accuracy and the kappa value increased by 5.43 percent and 0.08 when the H/A/Alpha decomposition was used in the proposed method. Furthermore, the user's accuracy for vegetation and the producer's accuracy for built-up area significantly improved when the H/A/Alpha decomposition was employed. As shown in Figure 3, α_2 and PH are important in distinguishing between vegetation and built-up areas; α_2 is related to the underlying average physical scattering mechanism of the observed targets, and PH is related to the randomness in the scattering. Buildings have the typical characteristics of double-bounce scattering, and forest and dense vegetation have the typical characteristics of volume scattering. Therefore, α_2 and PH are important in distinguishing between these two classes.

This proposed method was used for the classification by only using polarimetric decomposition and decision tree

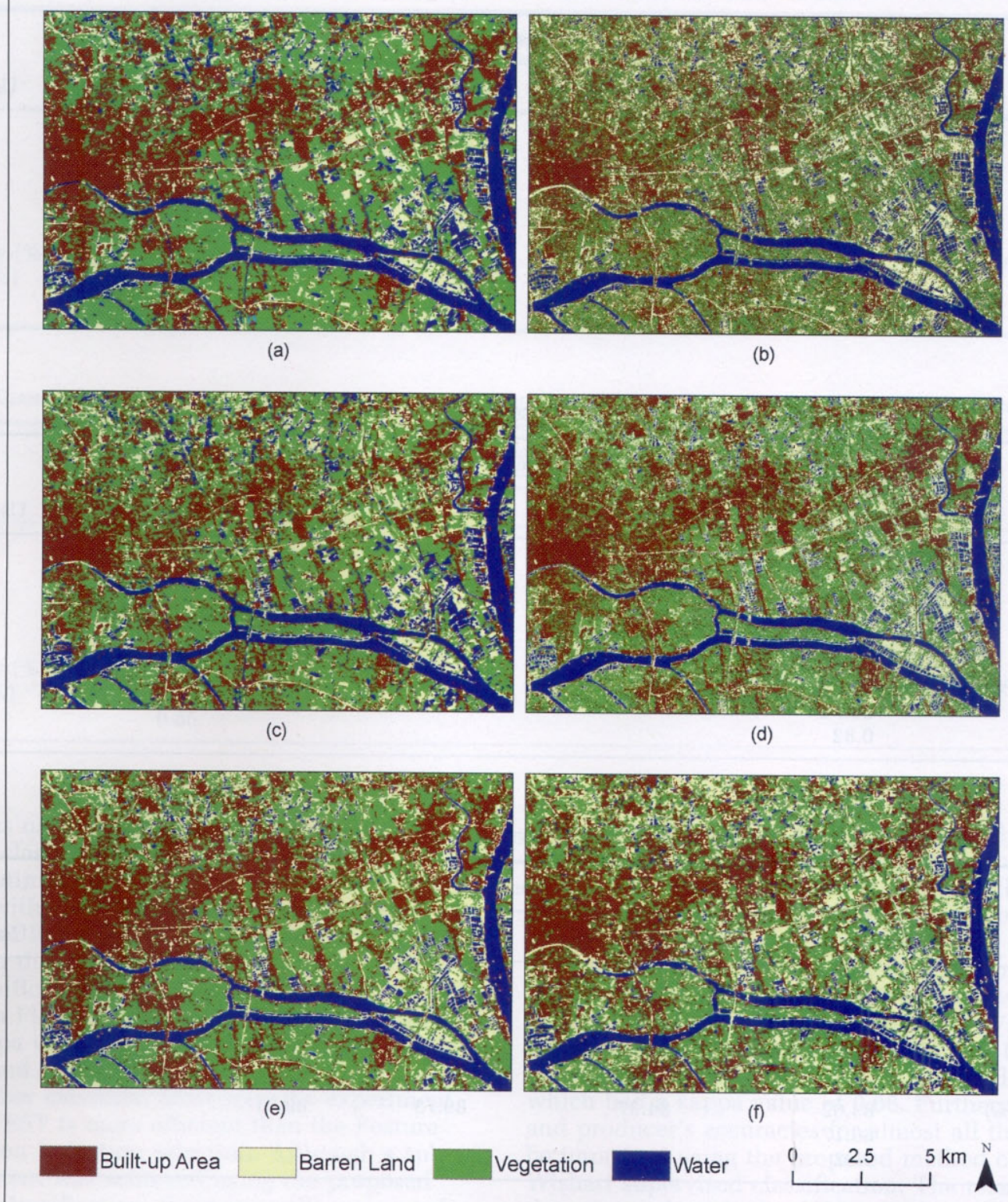

Plate 3. LULC classification results: (a) Proposed method, (b) Wishart supervised classification based on the coherency matrix, (c) Proposed method without the H/A/Alpha decomposition, (d) Proposed method without object-oriented image analysis, (e) Proposed method without incorporating textural and spatial information, and (f) Proposed method using the nearest neighbor classifier instead of decision tree algorithms.

TABLE 2. CLASSIFICATION ACCURACY OF THE PROPOSED METHOD

	Reference data					
Classified data	Barren Land	Built-up Area	Vegetation	Water	Total	User's Accuracy (%)
Barren Land	8,014	49	258	1,295	9,616	83.34
Built-up Area	236	8,309	422	170	9,137	90.94
Vegetation	25	398	9,061	0	9,484	95.54
Water	51	19	22	9,286	9,378	99.02
Total	8,326	8,775	9,763	10,751	37,615	
Producer's accuracy (%)	96.25	94.69	92.81	86.37		
Overall accuracy (%)	92.17					
Kappa	0.90					

TABLE 3. CLASSIFICATION ACCURACY OF THE WISHART SUPERVISED CLASSIFICATION

	Reference data					
Classified data	Barren Land	Built-up Area	Vegetation	Water	Total	User's Accuracy (%)
Barren Land	7,250	741	562	1,063	9,616	75.40
Built-up Area	269	7,920	783	165	9,137	86.68
Vegetation	1,070	3,777	4,637	0	9,484	48.89
Water	568	204	308	8,298	9,378	88.48
Total	9,157	12,642	6,290	9,526	37,615	
Producer's accuracy (%)	79.17	62.65	73.72	87.11		
Overall accuracy (%)	74.72					
Kappa	0.66					

TABLE 4. CLASSIFICATION ACCURACY OF THE PROPOSED METHOD WITHOUT THE H/A/ALPHA DECOMPOSITION

	Reference data					
Classified data	Barren Land	Built-up Area	Vegetation	Water	Total	User's Accuracy (%)
Barren Land	8,240	71	144	1,161	9,616	85.69
Built-up Area	236	8,321	410	170	9,137	91.07
Vegetation	559	2,150	6,775	0	9,484	71.44
Water	61	19	5	9,293	9,378	99.09
Total	9,096	10,561	7,334	10,624	37,615	
Producer's accuracy (%)	90.59	78.79	92.38	87.47		
Overall accuracy (%)	86.74					
Kappa	0.82					

TABLE 5. CLASSIFICATION ACCURACY OF THE PROPOSED METHOD WITHOUT OBJECT-ORIENTED IMAGE ANALYSIS

	Reference data					
Classified data	Barren Land	Built-up Area	Vegetation	Water	Total	User's Accuracy (%)
Barren Land	8,490	9	195	922	9,616	88.29
Built-up Area	206	8,160	595	176	9,137	89.31
Vegetation	512	1,500	7,472	0	9,484	78.79
Water	1,019	3	65	8,291	9,378	88.41
Total	10,227	9,672	8,327	9,389	37,615	
Producer's accuracy (%)	83.02	84.37	89.73	88.31		
Overall accuracy (%)	86.17					
Kappa	0.82					

algorithms but without object-oriented image analysis. The classification was implemented on a pixels basis, and only the value of pixels was utilized in the classification. The classification result and the accuracy evaluation are shown in Plate 3d and Table 5. The comparison between the method without object-oriented image analysis and the proposed method shows the contribution of object-oriented image analysis to the final accuracy of the proposed method. The overall accuracy and the kappa value increased by 6.00 percent and 0.08 when object-oriented image analysis was used in the proposed method. Besides of the increase in the overall accuracy and kappa value, the user's and producer's accuracies for almost all the classes increased when object-oriented image analysis was used. Moreover, the proposed method more effectively represented reality than did the pixel-based classification. Lower spatial heterogeneity is observed in Plate 3a than in Plate 3d because the proposed method was less affected by speckle in the POLSAR image compared with the pixel-based method. This minimal effect was achieved through the implementation of the classification based on image objects.

Classification using the proposed method without incorporating any textural or spatial features was conducted. The classification result and the accuracy evaluation are shown in Plate 3e and Table 6. The comparison between this classification and the classification using the proposed method shows the contribution of textural information to the final accuracy of the proposed method. The overall accuracy and the kappa value of the proposed method increased by 2.07 percent and 0.03 compared with the method without using textural and spatial information. Furthermore, the proposed method achieved higher user's accuracy for water and producer's accuracy for barren land. Figure 3 shows that the standard deviation of T_{13} and the GLCM Ang. 2nd moment of PH are helpful in distinguishing between water and barren land.

Classification using the proposed method integrating the nearest neighbor classifier instead of decision tree algorithms was carried out to investigate the contribution of decision tree algorithms to the final accuracy of the proposed method. The nearest neighbor classifier is commonly used for object-oriented classification. In this study, the nearest neighbor classification was implemented using Definiens Developer 7.0 (Baatz *et al.*, 2004). The Feature Space Optimization function provided by Definiens

TABLE 6. CLASSIFICATION ACCURACY OF THE PROPOSED METHOD WITHOUT INCORPORATING TEXTURAL AND SPATIAL INFORMATION

	Reference data					
Classified data	Barren Land	Built-up Area	Vegetation	Water	Total	User's Accuracy (%)
Barren Land	8,156	0	309	1,151	9,616	84.82
Built-up Area	236	8,297	434	170	9,137	90.81
Vegetation	25	393	9,066	0	9,484	95.59
Water	964	24	17	8,373	9,378	89.28
Total	9,381	8,714	9,826	9,694	37,615	
Producer's accuracy (%)	86.94	95.21	92.27	86.37		
Overall accuracy (%)	90.10					
Kappa	0.87					

TABLE 7. CLASSIFICATION ACCURACY OF THE PROPOSED METHOD USING THE NEAREST NEIGHBOR CLASSIFIER INSTEAD OF DECISION TREE ALGORITHMS

	Reference data					
Classified data	Barren Land	Built-up Area	Vegetation	Water	Total	User's Accuracy (%)
Barren Land	8,439	0	456	721	9,616	87.76
Built-up Area	235	8,044	686	172	9,137	88.04
Vegetation	542	252	8,690	0	9,484	91.63
Water	1,108	24	22	8,224	9,378	87.69
Total	10,324	8,320	9,854	9,117	37,615	
Producer's accuracy (%)	81.74	96.68	88.19	90.21		
Overall accuracy (%)	88.79					
Kappa	0.85					

Developer 7.0 was used to select the features used in the nearest neighbor classification (Baatz *et al.*, 2004). The Feature Space Optimization compares the samples for selected classes with respect to features, and determines the combination of features that produces the largest average minimum distance between the samples of different classes. The classification result and the accuracy evaluation are shown in Plate 3f and Table 7. The overall accuracy and the kappa value of the proposed method increased by 3.38 percent and 0.05 compared with the method using the nearest neighbor classifier. Moreover, the experiment indicates that QUEST is more efficient than the Feature Space Optimization in feature selection. Although a substantial improvement was achieved using the proposed method for LULC classification, there was still some confusion between different LULC classes in the classification. Some buildings with specific orientations that are not aligned in the azimuth direction or having complex structures such as rough roofs that backscatter polarized waves randomly were often confused with those from vegetation. Some buildings with wide flat roof tended to be confused with barren land because of the similar single-bounce scattering mechanism taking place on the flat roof and the barren land. The shadow of buildings was prone to be confused with barren land because of little radar return from both of them. The shadow of buildings was not illuminated by the sensor, and the barren land reflected most of the incident radar wave to the opposite direction. There was also confusion between the shadow of mountains and barren land for the same reason. Some barren land with water on their surface or high soil moisture was always confused with water.

Conclusions

LULC classification is an important research topic in the methodology and applications of remote sensing. This paper has proposed a new method that integrates polarimetric decomposition, object-oriented image analysis, and decision tree algorithms for LULC classification using RADARSAT-2 POLSAR data. The proposed method can achieve much higher overall accuracy and kappa value than the Wishart supervised classification which is based on the coherency matrix for the classification of POLSAR data. The overall accuracy of the proposed method was 92.17 percent, whereas that of the Wishart supervised classification was 74.72 percent. The kappa value of the proposed method was 0.90. It is much higher than that of the Wishart supervised classification, which had a kappa value of 0.66. Furthermore, the user's and producer's accuracies for almost all the LULC classes can be improved using the proposed method compared with the Wishart supervised classification. The results indicate that the proposed method exhibits much better performance than the Wishart supervised classification for LULC classification using POLSAR data.

Polarimetric decomposition, object-oriented image analysis, and decision tree algorithms all contribute to the improvement achieved by the proposed method. The overall accuracy and the kappa value of the proposed method will decrease by 5.43 percent and 0.08 if it is without the H/A/Alpha decomposition. The polarimetric parameters extracted using polarimetric decomposition techniques are related to the scattering properties of the observed objects; thus, they have significant implications for the classification of POLSAR data. The performance of the classification of POLSAR data can be improved by incorporating these polarimetric parameters into the classification. This study has shown that some polarimetric parameters, such as α_2 and PH, are important in distinguishing between vegetation and built-up area. The overall accuracy and the kappa value of the proposed method will decrease by 6.00 percent and 0.08 if it is without object-oriented image analysis. Object-oriented image analysis is helpful in improving the accuracy of the classification of POLSAR images by reducing the speckle effect and extracting textural and spatial information to support the classification. Some textural features, such as the standard

deviation of T_{13} and the GLCM Ang. 2nd moment of PH, are helpful in distinguishing between water and barren land. Moreover, the object-oriented classification of POLSAR data can exhibit better performance in terms of representing reality than does pixel-based classification, because it is less affected by speckle. The overall accuracy and the kappa value of the proposed method will decrease by 3.38 percent and 0.05 if it is based on the nearest neighbor classifier instead of decision tree algorithms. With the addition of polarimetric, textural, and spatial information, hundreds of features can be potentially incorporated into the object-oriented classification of POLSAR data. Decision tree algorithms can be used to select the most important features that achieve the best classification result. In this study, QUEST proved to be efficient in selecting features and implementing classification. Higher classification accuracy can be achieved using QUEST than when the nearest neighbor classifier is used.

LULC classification using only one RADARSAT-2 POLSAR image does not provide sufficient information for the accurate separation of different types of vegetation. The main problem is that polarimetric information is saturated with the increase in height and density of vegetation layer. One promising way to overcome this problem is to incorporate interferometric information into the classification. The magnitude of interferometric coherency, which is less affected by any amplitude saturation effects, allows high biomass forest classification even at higher frequencies (Lee and Pottier, 2009). Further studies will be conducted to incorporate interferometric information into the classification of POLSAR data to achieve more observation space and higher accuracy.

Acknowledgments

This study was supported by the National Basic Research Program of China (973 Program) (Grant No. 2011CB707103), the Key National Natural Science Foundation of China (Grant No. 40830532), and the Science and Operational Applications Research for RADARSAT-2 Program (SOAR 2762). The authors would like to thank the Canadian Space Agency (CSA) and the MDA Geospatial Services, Inc. for providing the RADARSAT-2 data.

References

Ainsworth, T.L., J.S. Lee, and D.L. Schuler, 2000. Multi-frequency polarimeric SAR data analysis of ocean surface features, *Proceedings of IGARSS 2000: IEEE International Geoscience and Remote Sensing Symposium*, 16-18 May, Honolulu, Hawaii, pp: 24–28.

Ainsworth, T.L., S.R. Cloude, and J.S. Lee, 2002. Eigenvector analysis of polarimetric SAR data, *Proceedings of IGARSS 2002: IEEE International Geoscience and Remote Sensing Symposium and 24th Canadian Symposium on Remote Sensing*, 24-28 June, Toronto, Canada, pp: 626–628.

Allain, S., L. Ferro-Famil, and E. Pottier, 2004. Two novel surface model based inversion algorithms using multi-frequency PolSAR data, *Proceedings of IGARSS 2004: IEEE International Geoscience and Remote Sensing Symposium,* 20-24 September, Alaska, pp: 823–826.

Baatz, M., U. Benz, S. Dehghani, M. Heynen, A. Höltje, P. Hofmann, I. Lingenfelder, M. Mimler, M. Sohlbach, and M. Weber, 2004. *eCognition Professional User Guide 4*, Definiens Imaging, Munich.

Barnes, C.F., and J. Burki, 2006. Late-season rural land-cover estimation with polarimetric-SAR intensity pixel blocks and sigma-tree-structured near-neighbor classifiers, *IEEE Transactions on Geoscience and Remote Sensing*, 44(9):2384–2392.

Benz, U.C., P. Hofmann, G. Willhauck, I. Lingenfelder, and M. Heynen, 2004. Multi-resolution, object-oriented fuzzy analysis of remote sensing data for GIS-ready information, *ISPRS Journal of Photogrammetry and Remote Sensing*, 58(3-4):239–258.

Cameron, W.L., and H. Rais, 2006. Conservative polarimetric scatterers and their role in incorrect extensions of the Cameron decomposition, *IEEE Transactions on Geoscience and Remote Sensing*, 44(12):3506–3516.

Carrea, L., and G. Wanielik, 2001. Polarimetric SAR processing using the polar decomposition of the scattering matrix, *Proceedings of IGARSS'01*, 09-13 July, Sydney, Australia, pp. 363–365.

Chen, K.S., W.P. Huang, D.H. Tsay, and F. Amar, 1996. Classification of multifrequency polarimetric SAR imagery using a dynamic learning neural network, *IEEE Transactions on Geoscience and Remote Sensing*, 34(3):814–820.

Cloude, S.R., and E. Pottier, 1996. A review of target decomposition theorems in radar polarimetry, *IEEE Transactions on Geoscience and Remote Sensing*, 34(2):498–518.

Cloude, S.R., and E. Pottier, 1997. An entropy based classification scheme for land applications of polarimetric SAR, *IEEE Transactions on Geoscience and Remote Sensing*, 35(1):68–78.

Congalton, R., and K. Green, 2009. *Assessing the Accuracy of Remotely Sensed Data: Principles and Practices*, CRC Press, Boca Raton, Florida, pp. 74–79.

Du, L., and J.S. Lee, 1996. Fuzzy classification of earth terrain covers using complex polarimetric SAR data, *International Journal of Remote Sensing*, 17(4):809–826.

Durden, S.L., J.J. Vanzyl, and H.A. Zebker, 1990. The unpolarized component in polarimetric radar observations of forested areas, *IEEE Transactions on Geoscience and Remote Sensing*, 28(2):268–271.

Evans, C., R. Jones, I. Svalbe, and M. Berman, 2002. Segmenting multispectral Landsat TM images into field units, *IEEE Transactions on Geoscience and Remote Sensing*, 40(5):1054–1064.

Ferro-Famil, L., E. Pottier, and J.S. Lee, 2001. Unsupervised classification of multifrequency and fully polarimetric SAR images based on the H/A/alpha-Wishart classifier, *IEEE Transactions on Geoscience and Remote Sensing*, 39(11):2332–2342.

Freeman, A., and S.L. Durden, 1998. A three-component scattering model for polarimetric SAR data, *IEEE Transactions on Geoscience and Remote Sensing*, 36(3):963–973.

Freitas, C.D., L. Soler, S.J.S. Sant'Anna, L.V. Dutra, J.R. dos Santos, J.C. Mura, and A.H. Correia, 2008. Land use and land cover mapping in the Brazilian Amazon using polarimetric airborne P-band SAR data, *IEEE Transactions on Geoscience and Remote Sensing*, 46(10):2956–2970.

Friedl, M.A., and C.E. Brodley, 1997. Decision tree classification of land cover from remotely sensed data, *Remote Sensing of Environment*, 61(3):399–409.

Gao, Y., J.F. Mas, B.H.P. Maathuis, X.M. Zhang, and P.M. Van Dijk, 2006. Comparison of pixel-based and object-oriented image classification approaches - A case study in a coal fire area, Wuda, Inner Mongolia, China, *International Journal of Remote Sensing*, 27(18):4039–4055.

Geneletti, D., and B.G.H. Gorte, 2003. A method for object-oriented land cover classification combining Landsat TM data and aerial photographs, *International Journal of Remote Sensing*, 24(6):1273–1286.

Hara, Y., R.G. Atkins, S.H. Yueh, R.T. Shin, and J.A. Kong, 1994. Application of neural networks to radar image classification, *IEEE Transactions on Geoscience and Remote Sensing*, 32(1):100–109.

Henderson, F.M., 1975. Radar for small-scale land-use mapping, *Photogrammetric Engineering & Remote Sensing*, 41(3):307–319.

Henderson, F.M., 1977. Land-use interpretation with radar imagery, *Photogrammetric Engineering & Remote Sensing*, 43(1):95–99.

Henderson, F.M., 1979. Land-Use analysis of radar imagery, *Photogrammetric Engineering & Remote Sensing*, 45(3):295–307.

Huynen, J.R., 1970. *Phenomenological Theory of Radar Targets*, Ph.D. dissertation, Drukkerij Bronder-offset N. V., Rotterdam.

Imhoff, M.L., W.T. Lawrence, D.C. Stutzer, and C.D. Elvidge, 1997. A technique for using composite DMSP/OLS "city lights" satellite data to map urban area, *Remote Sensing of Environment*, 61(3):361–370.

Kandrika, S., and P.S. Roy, 2008. Land use land cover classification of Orissa using multi-temporal IRS-P6 AWIFS data: A decision tree approach, *International Journal of Applied Earth Observation and Geoinformation*, 10(2):186–193.

Kasischke, E.S., J.M. Melack, and M.C. Dobson, 1997. The use of imaging radars for ecological applications - A review, *Remote Sensing of Environment*, 59(2):141–156.

Laliberte, A.S., J. Koppa, E.L. Fredrickson, and A. Rango, 2006. Comparison of nearest neighbor and rule-based decision tree classification in an object-oriented environment, *Proceedings of 2006 IEEE International Geoscience and Remote Sensing Symposium*, 31 July-04 August, Denver, Colorado, pp: 3923–3926.

Lawrence, R.L., and A. Wright, 2001. Rule-based classification systems using classification and regression tree (CART) analysis, *Photogrammetric Engineering & Remote Sensing*, 67(10): 1137–1142.

Lee, J.S., M.R. Grunes, and R. Kwok, 1994. Classification of multi-look polarimetric SAR imagery-based on complex Wishart distribution, *International Journal of Remote Sensing*, 15(11):2299–2311.

Lee, J.S., M.R. Grunes, T.L. Ainsworth, L.J. Du, D.L. Schuler, and S.R. Cloude, 1999a. Unsupervised classification using polarimetric decomposition and the complex Wishart classifier, *IEEE Transactions on Geoscience and Remote Sensing*, 37(5):2249–2258.

Lee, J.S., M.R. Grunes, and G. de Grandi, 1999b. Polarimetric SAR speckle filtering and its implication for classification, *IEEE Transactions on Geoscience and Remote Sensing*, 37(5): 2363–2373.

Lee, J.S., M.R. Grunes, and E. Pottier, 2001. Quantitative comparison of classification capability: Fully polarimetric versus dual and single-polarization SAR, *IEEE Transactions on Geoscience and Remote Sensing*, 39(11):2343–2351.

Lee, J.S., and E. Pottier, 2009. *Polarimetric Radar Imaging from Basics to Applications*, CRC Press, New York, pp. 179–264.

Leiss, I.A., S. Sandmeier, K.I. Itten, and T.W. Kellenberger, 1996. Use of expert knowledge and possibility theory in land use classification, *Progress in Environmental Remote Sensing Research and Applications*, pp. 133–137.

Li, X., and A.G. Yeh, 2004. Multitemporal SAR images for monitoring cultivation systems using case-based reasoning, *Remote Sensing of Environment*, 90(4):524–534.

Li, H.T., H.Y. Gu, Y.S. Han, and J.H. Yang, 2008. Object-oriented classification of polarimetric SAR imagery based on statistical region merging and support vector machine, *Proceedings of 2008 International Workshop on Earth Observation and Remote Sensing Applications*, 30 June-02 July, Beijing, China, pp. 147–152.

Li, X., A.G.O. Yeh, J.P. Qian, B. Ai, and Z.X. Qi, 2009. A matching algorithm for detecting land use changes using case-based reasoning, *Photogrammetric Engineering & Remote Sensing*, 75(11):1319–1332.

Lim, T.S., W.Y. Loh, and Y.S. Shih, 2000. A comparison of prediction accuracy, complexity, and training time of thirty-three old and new classification algorithms, *Machine Learning*, 40(3):203–228.

Loh, W.Y., and Y.S. Shih, 1997. Split selection methods for classification trees, *Statistica Sinica*, 7(4):815–840.

Luneburg E., 2001. Foundations of the mathematical theory of polarimetry, *Final Report, Phase I, N00014-00-M-0152*, EML Consultants.

López-Martínez, C., L. Ferro-Famil, and E. Pottier, 2005. PolSARpro, version 4.0, Polarimetry Tutorial, URL: *http://earth.esa.int/polsarpro/tutorial.html*, European Space Agency, Paris, France (last date accessed: 28 September 2011).

McCoy, R.M., 2005. *Field Methods in Remote Sensing*, The Guilford Press, New York, pp. 18–19.

McIver, D.K., and M.A. Friedl, 2002. Using prior probabilities in decision-tree classification of remotely sensed data, *Remote Sensing of Environment*, 81(2-3):253–261.

Pierce, L.E., F.T. Ulaby, K. Sarabandi, and M.C. Dobson, 1994. Knowledge-based classification of polarimetric SAR images, *IEEE Transactions on Geoscience and Remote Sensing*, 32(5):1081–1086.

Pierce, L.E., K.M. Bergen, M.C. Dobson, and F.T. Ulaby, 1998. Multitemporal land-cover classification using SIR-C/X-SAR imagery, *Remote Sensing of Environment*, 64(1):20–33.

Pottier, E., and J.S. Lee, 1999. Application of the "H/A/Alpha" polarimetric decomposition theorem for unsupervised classification of fully polarimetric SAR data based on the Wishart distribution, *Proceedings of CEOS SAR Workshop*, 26-29 October, Toulouse, France, pp. 335–340.

Pottier, E., J.S. Lee, and L. Ferro-Famil, 2005. PolSARpro, version 3.0, Lecture Notes – Advanced concepts, URL: *http://earth.esa.int/polsarpro/tutorial.html*, European Space Agency, Paris, France (last date accessed: 28 September 2011).

Refregier, P., and J. Morio, 2006. Shannon entropy of partially polarized and partially coherent light with Gaussian fluctuations, *Journal of the Optical Society of America a-Optics Image Science and Vision*, 23(12):3036–3044.

Ridd, M.K., and J.J. Liu, 1998. A comparison of four algorithms for change detection in an urban environment, *Remote Sensing of Environment*, 63(2):95–100.

Rignot, E., R. Chellappa, and P. Dubois, 1992. Unsupervised segmentation of polarimetric SAR data using the covariance-matrix, *IEEE Transactions on Geoscience and Remote Sensing*, 30(4):697–705.

Saatchi, S.S., J.V. Soares, and D.S. Alves, 1997. Mapping deforestation and land use in Amazon rainforest by using SIR-C imagery, *Remote Sensing of Environment*, 59(2):191–202.

Story, M., and R.G. Congalton, 1986. Accuracy assessment: A user's perspective, *Photogrammetric Engineering & Remote Sensing*, 52(3):397–399.

Sutton, P.C., 2003. A scale-adjusted measure of "urban sprawl" using nighttime satellite imagery, *Remote Sensing of Environment*, 86(3):353–369.

Swain, P.H., and H. Hauska, 1977. Decision tree classifier - Design and potential, *IEEE Transactions on Geoscience and Remote Sensing*, 15(3):142–147.

Tzeng, Y.C., and K.S. Chen, 1998. A fuzzy neural network to SAR image classification, *IEEE Transactions on Geoscience and Remote Sensing*, 36(1):301–307.

Uchiyama, T., and M.A. Arbib, 1994. An algorithm for competitive learning in clustering problems, *Pattern Recognition*, 27(10):1415–1421.

Ulaby, F.T., F. Kouyate, B. Brisco, and T.H.L. Williams, 1986. Textural information in SAR images, *IEEE Transactions on Geoscience and Remote Sensing*, 24(2):235–245.

Van Zyl, J.J., 1992. Application of Cloude's target decomposition theorem to polarimetric imaging radar data, *SPIE*, 127:184–212.

Watts, J.D., R.L. Lawrence, P.R. Miller, and C. Montagne, 2009. Monitoring of cropland practices for carbon sequestration purposes in north central Montana by Landsat remote sensing, *Remote Sensing of Environment*, 113(9):1843–1852.

Wu, S.S., X.M. Qiu, E.L. Usery, and L. Wang, 2009. Using geometrical, textural, and contextual information of land parcels for classification of detailed urban land use, *Annals of the Association of American Geographers*, 99(1):76–98.

Yang, J., Y. Yamaguchi, H. Yamada, M. Sengoku, and S.M. Lin, 1998. Stable decomposition of Mueller matrix, *IEICE Transactions on Communications*, E81b(6):1261–1268.

(Received 05 May 2010; accepted 18 May 2011; final version 23 June 2011)